Article

Transition-Metals Doped TiO_2 Nanoparticles Supported on Zeolite Y with Photocatalytic Properties

Gabriela Petcu[1], Florica Papa[1], Irina Atkinson[1], Adriana Baran[1], Nicoleta G. Apostol[2], Simona Petrescu[1], Lionel Richaudeau[3], Jean-Luc Blin[3,*] and Viorica Parvulescu[1]

[1] Institute of Physical Chemistry "Ilie Murgulescu" of the Romanian Academy, Bucharest, Romania; gpetcu@icf.ro (G.P.); iatkinson@icf.ro (I.A.); floricapapa@gmail.com (F.P.); adibaran@gmail.com (A.B.); simon_pet@yahoo.com (S.P.); vpirvulescu@icf.ro(V.P.)

[2] National Institute of Materials Physics, Atomiștilor 405A, 077125 Măgurele – Ilfov, Romania; nicoleta.apostol@infim.ro(N.G.A.)

[3] Université de Lorraine, CNRS, L2CM, F-54000 Nancy, France; jean-luc.blin@univ-lorraine.fr. (J.-L.B.); lionel.richaudeau@univ-lorraine.fr (L.R.)

* Correspondence: jean-luc.blin@univ-lorraine.fr. (J.-L.B.)

Abstract: Zeolite Y with microporous and hierarchical structure containing Ti–Ni and Ti–Co oxides were obtained as active photocatalysts. Different Ti amounts (5, 10% TiO_2) were supported, followed by loading of Ni or Co oxides (5 %). The X-ray diffraction evidenced the presence of TiO_2 as anatase. N_2 adsorption-desorption results showed type IV isotherms, for hierarchical zeolite Y samples, and a combination of type IV and I isotherms, for zeolite Y samples. UV–Vis diffuse reflectance spectra showed shift of absorption band to visible with increasing of Ti loading and especially after Co and Ni addition. A significant effect of the support was evidenced for Ti and interaction with Co/Ni species. The zeolite Y support stabilizes Ti in the 4+ oxidation state while hierarchical zeolite Y support favored the formation of Ti 3+ species and oxidation of Co and especially of Ni to 3+. Photocatalytic activity, under UV and visible light, was evaluated in degradation of amoxicillin, used as a model test. The photocatalytic mechanism was investigated using ethanol, p-benzoquinone and KI as ·OH, $\cdot O_2^-$ radicals and hole (h^+) scavengers. The best results were obtained for the immobilized Ni-Ti species on hierarchical zeolite Y support.

Keywords: Co-Ti/ zeolite Y; Ni-Ti/zeolite Y; hierarchical zeolite Y; properties; photodegradation; amoxicillin; UV light; visible light; scavengers; mechanism

1. Introduction

The use of zeolite-based materials as adsorbents and photocatalysts for the extraction of heavy metals and degradation of wide variety of dyes, pharmaceutical compounds like antibiotics and other organic pollutants was broadly discussed [1-4], highlighting the advantage of their use in the treatment of contaminated water. Zeolites offer high surface area, nanoporous structure, strong acidity, high ion exchange ability and hydrothermal stability for synthesis of highly efficient photocatalysts. Unfortunately, the micropores from zeolites and active sites from the surface are less accessible to organic pollutants due to the limitations of mass transport. Furthermore, materials with a mesoporous structure are widely used as a support in the synthesis of photocatalysts because of their highly ordered mesoporous channels and large surface area [5, 6, 7]. The solution to keep the properties of zeolites, along with the advantage of mass transfer through mesopores, seems to be hierarchical zeolites. These materials have significant advantages in reactions involving large molecules by coupling the native micropores with intracrystalline mesopores network. Higher adsorption capacity and degradation efficiency of amoxicillin were obtained for Au-Ti [7] and Fe–Ti [8] bimetallic photocatalysts supported on hierarchical zeolites Y photocatalysts. Whereas all the

Preprints (www.preprints.org) | NOT PEER-REVIEWED | Posted: 15 June 2023 doi:10.20944/preprints202306.1109.v1

zeolite supports are not photoactive they were activated by incorporation of semiconductors and metal nanoparticles. The preparation of nanocomposite photocatalysts by immobilization of nanosized titanium dioxide into zeolite is a very promising solution to removal of organic and inorganic pollutants from water [4,9-11]. The utilization of zeolite as a carrier for titanium dioxide led to smaller particle sizes of this oxide. Also, the photocatalytic activity of the TiO_2-zeolite system increased comparatively to that of TiO_2. However, TiO_2 is a wide band gap semiconductor (~3.2 eV) and high recombination rate for electron-hole pairs with limited practical utility [12, 13]. Recently, there has been increased the interest in the synthesis of nanocomposite materials as photocatalysts more efficient and active under visible light irradiation by doping of TiO_2 with noble metals [7, 14, 15] and transition metals semiconductors [8, 16-19]. The increase of catalytic activity with transition metals is alternative to highly expensive noble metals. The transition metal cations have been found to be dopants and cocatalysts in the photocatalytic reactions. Among different transition metal ions, Ni and Co attracted attention for the development of visible light active TiO_2 materials used in photocatalytic degradation of organic pollutants [20-27]. At the interfacial contact between n-type TiO_2 semiconductor and a p semiconductor as nickel and cobalt oxides is established an p-n heterojunction which represents an effective way to hinder electron hole pair recombination after light absorption and prolong the charge carrier life time [28-30]. Theoretically, the p–n junction generates an internal electric field at the interface, which causes, at equilibrium, a negative charge in p-type semiconductor region while the TiO_2 region has a positive charge [28]. Under the illumination, the photogenerated electron-hole pairs are separated by the internal electric field. Thus the electrons move in the positive field and the holes in the negative field. Their separation leads to a significant increase in photocatalytic activity.

Cobalt oxide was reported as good photocatalyst for pollutants degradation [5]. Bahnemann et al. [22] highlighted the effect of the synthesis method on the photocatalytic activity of TiO_2 doped with cobalt. It was also shown that the photocatalytic activity under visible light irradiation depends largely on the valence state of the Co ions in the dopant and its concentration rather than the specific surface area of the support and the crystallinity of the anatase [5,21]. Also, in the case of TiO_2 doping with NiO, it was evidenced [29] that the synergistic interactions of heterojunctions, design, synthesis method, and structure influenced the photocatalytic performances. PL spectra [31] showed that the small amount of Ni on TiO_2 enhances the recombination of photogenerated electrons and holes and Ni excess decrease reaction rate, due to coverage effect of nickel species on the active site from titanium bioxide surface.

While, most of the works have been focused on modifying TiO_2 based photocatalysts in order of their increasing efficiency in degradation of pollutants under sunlight or visible light irradiation a limited number had as their objective the activation of zeolite type supports and especially hierarchical zeolites. Also, a comparative study of the effect of Co and Ni doping on the activity of TiO_2 immobilized on a zeolite support with a micro-mesoporous structure has not been carried out. The novelty also consists in evaluation with scavengers of the photocatalytic reactions mechanism.

In this work were studied zeolites Y containing Ti–Ni and Ti–Co mixed oxides as photocatalysts for degradation of amoxicillin from water. The zeolite Y supports, with microporous and hierarchical structure, were synthesized and impregnated, as active species, with different Ti amounts (5%, 10% TiO_2) followed of Ni or Co species (5% NiO, CoO) loading. The effects of supports, TiO_2 loading and type of the second immobilized metal (Ni or Co) on formation of reactive species, photocatalytic performances and mechanism were studied.

2. Materials and Methods

2.1. Materials

Sodium silicate solution ($Na_2O(SiO_2)_x \cdot xH_2O$, reagent grade), sodium aluminate ($NaAlO_2$), sodium hydroxide (NaOH, ≥98 %), 1-propanol ($CH_3CH_2CH_2OH$, ACS reagent, ≥99.5 %), tetradecyltrimethylammonium bromide—TTAB ($CH_3(CH_2)_{13}N(Br)(CH_3)_3$, for synthesis), amoxicillin ($C_{16}H_{19}N_3O_5S$, 95.0–102.0% anhydrous basis) used for photocatalytic reactions, and terephthalic acid

Preprints (www.preprints.org) | NOT PEER-REVIEWED | Posted: 15 June 2023 doi:10.20944/preprints202306.1109.v1

(98%) were purchased from Sigma Aldrich (Burlington, MA, USA), titanium (IV) n-butoxide ($Ti(OCH_2CH_2CH_2CH_3)_4$, reagent grade, 97%) from ACROS Organics (Geel, Belgium), nickel (II) nitrate ($(Ni(NO_3)_2 \cdot 6H_2O)$) and cobalt (II) nitrate ($(Co(NO_3)_2 \cdot 6H_2O)$) from Merck (Darmstadt, Germany). Potassium iodide (KI) ethanol (C_2H_5OH), p-benzoquinone ($C_6H_4O_2$) used as scavengers were purchased from Merck.

2.2. Photocatalysts Preparation

Hierarchical zeolite Y (noted hY) was obtained by a seed assisted method, previously reported [16], in the presence of TTAB as mesopores structure directing agent. After 24 hours of aging, the synthesis mixture with the molar ratio $0.66Na_2O:0.21Al_2O_3:SiO_2:0.02TTAB:19.1H_2O$ was hydrotermally treated for 6 hours at 100 °C. Zeolite Y having only microporous structure (noted Y) was obtained in a similar way, but in the absence of surfactant. The precipitates obtained after the hydrothermal treatment were filtered, washed with deionized water until pH=9, dried at 60 °C and calcined at 600 °C, 6 hours.

Modification of zeolite Y and hierarchical zeolite Y with titanium dioxide was carried out by impregnation with an alcoholic solution of titanium butoxide. In the case of zeolite Y, the concentration of the immobilized TiO_2 was 5%, while for the hierarchized zeolite hY, the percentage of TiO_2 was varied (2, 5 and 10%). After impregnation, the samples were dried at room temperature for 24 h and then at 80 °C for 12 hours. Calcination was carried out in air for 6 hours at 600 °C *with a heating rate of 2 °C/min*. Further, these materials were impregnated with aqueous solution of $Co(NO_3)_2$ or $Ni(NO_3)_2$, prepared so that the mass percentage of metal oxide in the final powders to be 5%. After impregnation, the samples were dried at room temperature for 24 hours and then at 60 °C for 8 hours. Calcination was carried out in air for 6 hours at 450 °C *with a heating rate of 2 °C/min*. The obtained materials were noted hYT2C, hYT5C, YT5C, hYT10C in the case of Ti and Co oxides modification and hYT2N, hYT5N, YT5N, hYT10N for Ti and Ni oxides modified materials.

2.3. Photocatalysts Characterization

X-ray diffraction (XRD) patterns were recorded using a Rigaku Ultima IV diffractometer (Rigaku Corp., Tokyo, Japan) with Cu Kα, λ = 0.15406 nm. Phase analysis was performed using Rigaku PDXL software with Whole Powder Pattern Fitting (WPPF) module, connected to the database ICDD-PDF-2.

Textural properties were evaluated from TRISTAR 3000 sorptometer (Micromeritics, Merignac, France). Before measurements, the samples were outgassed under vacuum (pressure = 0.13 mBar) at 25 °C for 16 h.

The scanning electron microscopy (SEM) with EDX, FEI Quanta 3D FEG was used to analyze the morphology and composition of the samples.

UV-Vis diffuse reflectance spectra of the powders were recorded in the 250-900 nm wavelength range using a JASCO V570 spectrophotometer (Tokyo, Japan).

Hydrogen temperature-programmed reduction (H_2-TPR) experiments were performed using a ChemBET 3000-Quantachrome instrument (USA) equipped with a thermal conductivity detectors (TCD). 50 mg of photocatalyst was used and a continuous flow of 5 vol% H_2 in Ar (70 mL/min). The heating rate was 10 °C/min, up to 850°C. In order to remove the water vapor and ensure optimal stability of the TCD (thermal conductivity detector) a silica gel column was inserted.

The analysis of the surface of the samples was investigated by X-Ray Photoelectron Spectroscopy (XPS). XPS spectra were obtained in an AXIS Ultra DLD (Kratos Surface Analysis, Manchester, UK) setup, using Al Kα1 (1486.74 eV) radiation produced by a monochromatized X-Ray source at operating power of 192 W and the high resolution core level spectra were recorded using hybrid lens mode, 40 eV pass energy, slot aperture. The binding energy scale was calibrated to the C 1s standard value of 284.6 eV and the spectra of interest were deconvoluted using Voigt profiles, based on the methods described in ref. [32].

Raman Scattering Spectra were collected on a Jobin-Yvon T64000 spectrometer equipped with an optical microscope in confocal mode (Horiba Jobin-Yvon, Palaiseau, France).

Preprints (www.preprints.org) | NOT PEER-REVIEWED | Posted: 15 June 2023 doi:10.20944/preprints202306.1109.v1

2.4. Photocatalystic Properties

The ability of the samples to generate, under irradiation, hydroxyl radicals in aqueous solution was evaluated with terephthalic acid. Thus, the fluorescence of the 2-hydroxyterephthalic acid (TAOH) resulting from the interaction of terephthalic acid (TA, 5×10^{-4} M TA prepared using an aqueous solution of NaOH 2×10^{-3} M) with hydroxyl radicals generated under irradiation by the samples (λ_{exc}=312 nm) was recorded using a spectrofluorometer FluoroMax 4P (Horiba Jobin Yvon, Northampton, UK).

The photocatalytic experiments were carried out in quartz microreactors, thermostated conditions (30 °C) and under stirring. Firstly, the amoxicillin aqueous solution (30 mg/L) and 20 mg of the photocatalyst were stirred for 30 minutes in darkness to allow AMX adsorption on the photocatalyst surface. Irradiation was then carried out for 5 hours, using 2 x 60 W halogen lamps. After 1, 3, and 5 hours of irradiation, 3 mL from reaction mixture was taken out, the photocatalyst was separated using Millipore syringe filter of 0.45 μm and the solution was spectrophotometrically measured using a JASCO V570 UV-Vis spectrophotometer (λ = 230 nm). AMX degradation was calculated using the solution phase concentration C_t (mg/L) at moment t and the initial concentration C_0 (mg/L) at t = 0.

In the case of ROS-scavenging tests, the experimental procedure was similar as in a photocatalytic test. In each reaction system was added 0.1 mmol of scavenger.

3. Results

3.1. Characterization of the samples

3.1.1. X-Ray Diffraction

The wide angle XRD patterns of the synthesited samples are illustrated in Figure 1 (a-b). For all the samples was evidenced the diffraction pattern of zeolite Y (ICDD 00-038-0239), used as support to obtain the photocatalysts. Furthermore, for all the prepared samples, was noticed a diffraction peak located at 25.2°, assigned to anatase [33] whose intensity increases with TiO_2 concentration (from 2% to 10%), most likely as a result of the size variation of the supported TiO_2 nanoparticles. The X-ray diffractograms presented in Figure 1a confirmed the presence of nickel as NiO species in the samples after inpregnation, by the appearance of characteristic diffraction lines at 37.3°, 43.3° and 62.9° [34]. In the case of modification with cobalt, XRD results suggest the formation of Co_3O_4 (Figure 1b), associated with the presence of some discrete diffraction peaks located at values of 2θ = 31.2°, 36.7° and 65.7° (ICDD 00-042-1467).

Preprints (www.preprints.org) | NOT PEER-REVIEWED | Posted: 15 June 2023 doi:10.20944/preprints202306.1109.v1

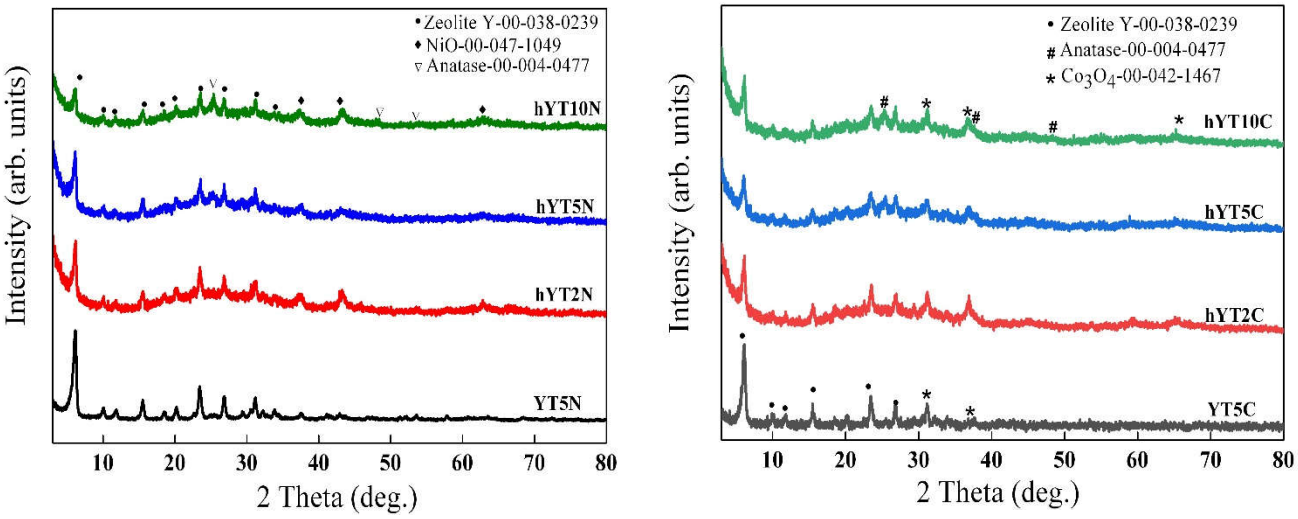

(a) (b)

Figure 1. X-ray diffractograms of (a) Ni-Ti/zeolite Y and (b) Co-Ti/zeolite Y samples (Y- zeolite Y with microporous structure, and hY-zeolite Y with hierarchical structure).

3.1.2. N_2-sorption

The nitrogen adsorption-desorption isotherms recorded for the materials obtained by impregnation with titania and nickel or cobalt oxide are shown in Figure 2.

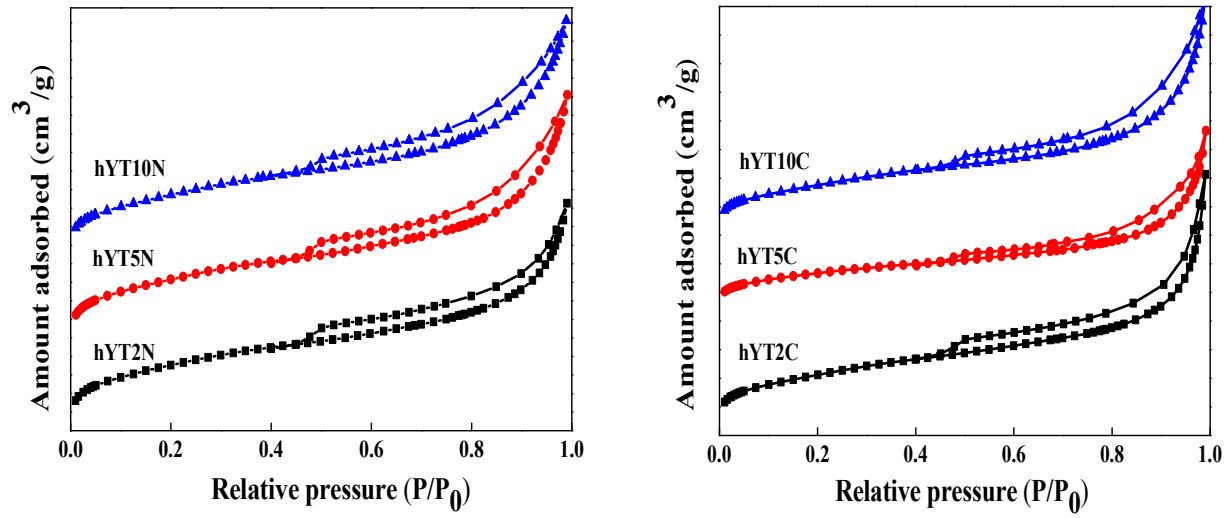

(a) (b)

Figure 2. The nitrogen adsorption–desorption isotherms of the zeolitic samples modified with (a) Ti-Ni oxides, and (b) Ti-Co oxides.

No change in the isotherm type, which is characteristic of the hY support (type IV) was evidenced after double impregnation processes (Figure 2). The specific surface area and pore volume values are shown in Table 1.

Preprints (www.preprints.org) | NOT PEER-REVIEWED | Posted: 15 June 2023 doi:10.20944/preprints202306.1109.v1

Table 1. The specific BET surface areas (S_{BET}), pore volume (V_{pore}), and band gap values of the synthesized photocatalysts.

Sample	hY	hYT2N	hYT5N	hYT 10N	hYT2C	hYT5C	hYT 10C
S_{BET} (m^2/g)	810	100	98	91	99	50	89
V_{pore} (cm^3/g)	0.2	0.08	0.08	0.08	0.1	0.06	0.09
E_g (eV)	-	2.18	2.93	2.88	1.55	2.51	2.05

A significant decrease of the specific surface after double impregnation with metal oxides was revealed, suggesting the blocking of the pores by the distribution of active species inside the micro- and mesopores.

3.1.3. Scanning Electron Microscopy (SEM)

Morphology of the modified zeolite supports with Co-Ti or Ni-Ti was evaluated by scanning electron microscopy (Figure 3). No change of morphology was observed after the impregnations of support. Thus, the preservation of octahedral morphology with smooth surface, specific to zeolite Y and no aggregates or any other observable defects in the structure of zeolite Y was evidenced.

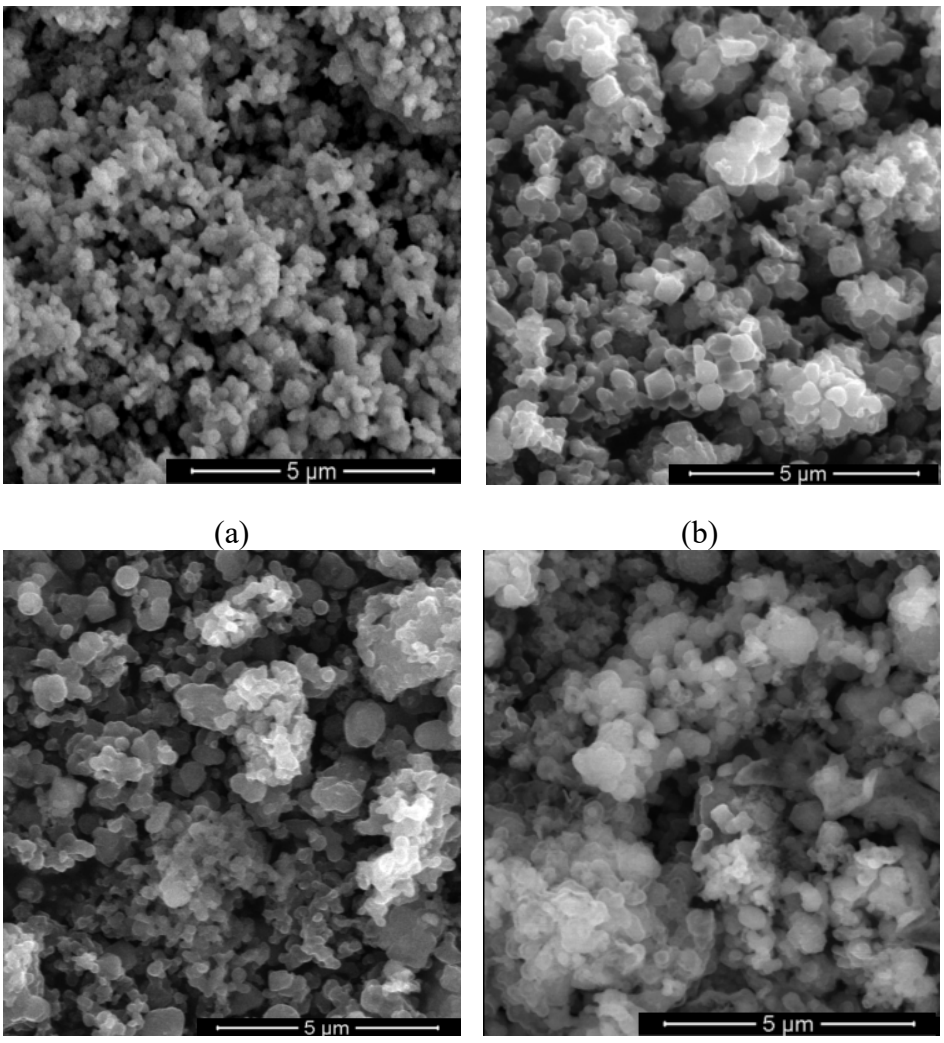

(a) (b)

(c) (d)

Preprints (www.preprints.org) | NOT PEER-REVIEWED | Posted: 15 June 2023 doi:10.20944/preprints202306.1109.v1

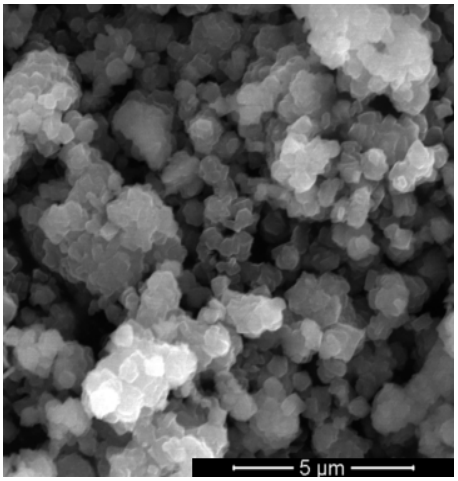

(e)

Figure 3. SEM images of (a) hYT2N, (b) hYT10N, (c) hYT10C, (d) hYT5C, and (e) YT5C samples.

The composition of the samples was evaluated by EDX analysis. The elemental analysis (Figure 4) shows the presence of immobilized species Ti, Co or Ti, Ni (Figure 4) and a higher content of elements (O, Si, Al, Na) from the composition of the zeolite supports.

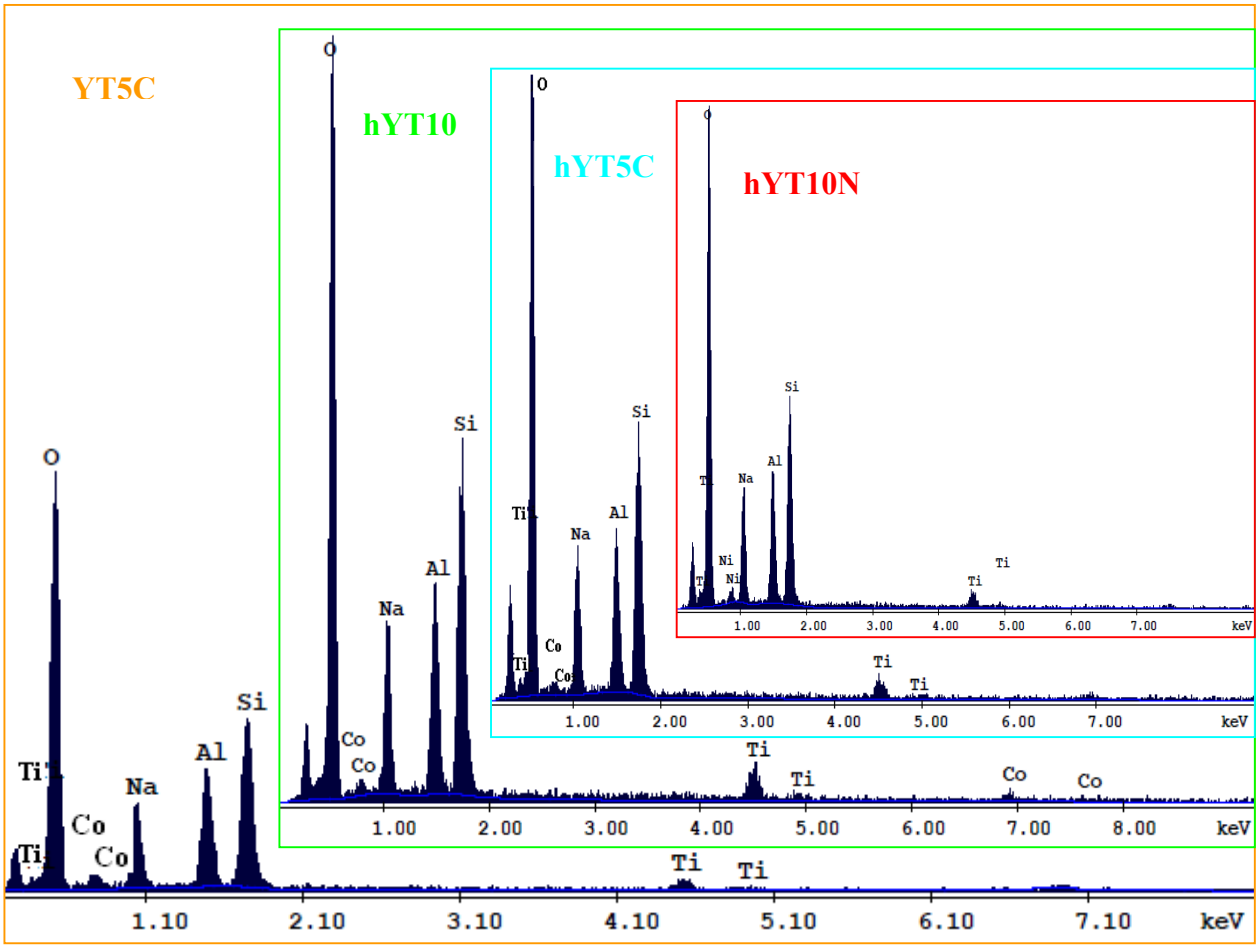

Figure 4. EDX spectrum of Co-Ti and Ni-Ti supported samples.

Preprints (www.preprints.org) | NOT PEER-REVIEWED | Posted: 15 June 2023 doi:10.20944/preprints202306.1109.v1

3.1.4. UV-Vis absorption spectroscopy

The optical properties of the samples were investigated by UV-Vis absorption spectroscopy, the results are shown in Figure 5. It was evidenced the presence of a broad absorption band for all the samples in the UV range, with a maximum peak located at ~ 260 nm, assigned to ligand-to-metal charge transfer of the highly dispersed octahedrally coordinated titanium oxide species. By increasing the TiO_2 amount from 2% to 10%, it can be noticed a broadening of the UV absorption band towards wavelengths over 300 nm, most likely due to the growing of the anatase particles size [35, 36].

Furthermore, in the case of Co-modified samples (Figure 5a), it was noticed the presence of two absorption bands in the visible domain, specific to Co_3O_4 species, with maxima located at ~440 nm and ~710 nm [37]. These are assigned to $O^{2-} \rightarrow Co^{2+}$ and $O^{2-} \rightarrow Co^{3+}$ charge transfer and also to $1A_{1g} \rightarrow 1T_{2g}$ electron transfer given by the octahedral Co(III) species. The hypsochromic shift of the characteristic absorption band of unsupported Co_3O_4 (located at 470 nm, as reported in the literature) indicates the obtaining of smaller sized Co_3O_4 species by dispersion on the Y zeolitic support [38]. The same behavior was observed for the Ni-modified samples which exhibited a broad absorption band with the maximum located at ~715 nm, assigned to NiO species (Figura 5b) and not at 725 nm, as was reported for the unsupported NiO [39].

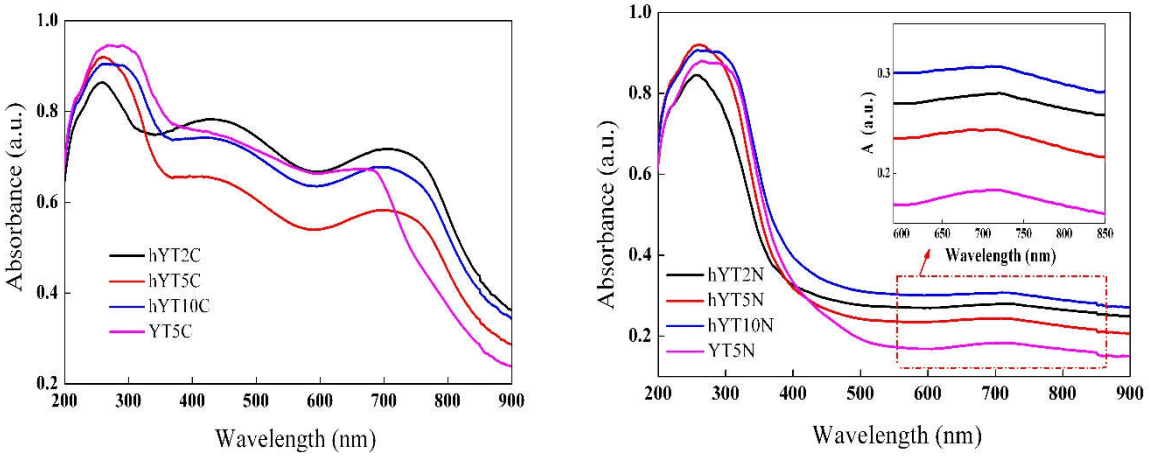

Figure 5. UV-Vis absorption spectra of (a) Ti-Co modified samples and (b) Ti-Ni modified samples.

The recorded UV-Vis absorption spectra indicate that the synthesized materials are active both in UV and visible light irradiation. Obtaining materials with visible light absorption capacity by modifying the zeolitic supports with Co or Ni oxide is an extremely important aspect in the current context where the maximization of efficiency is desired, but with minimal energy consumption [40] and was also supported by the band gap values calculated using the Kubelka-Munk function (Table 1).

3.1.5. H_2-TPR measurements

The reduction behavior of the synthesized photocatalysts was studied by thermoreduction measurements H_2-TPR to investigate the chemical state of the metal as well as to obtain information about the reducibility of the species on the photocatalyst surface and in the bulk. A strong interaction of the immobilized metal species with hierarchical zeolite Y can lead to changes in chemical status. A weak interaction with the support favors the reduction of metal oxides at lower temperatures, while the strong interaction with the support forms species that reduce at higher temperatures. The amount of H_2 (μmol) consumed per gram of photocatalyst is indicated in Table 2.

Preprints (www.preprints.org) | NOT PEER-REVIEWED | Posted: 15 June 2023 doi:10.20944/preprints202306.1109.v1

Table 2. The amount of hydrogen consumed, calculated from the TPR profiles of the samples.

Sample	The metallic species	μmol H_2/ g
YT5C	Co^{2+}, Co^{3+}	1109
YT5N	Ni^{2+}, Ni^{0}	869
hYT10C	Co^{2+}, Co^{3+}, Ti^{4+}, Ti^{3+}	1151
hYT10N	Ni^{2+},Ni^{0}	916
hYT5N	Ti^{4+},Ti^{3+}	858
hYT5C	Co^{3+}, Co^{2+}	1090

The TPR profiles recorded for the samples are illustrated in Figure 6 (a-b). In the case of materials modified with Ti and Ni oxides, the TPR profiles (Figure 6a) show several signals which can be divided as follows: peaks occurring at temperatures below 500 ° C are attributed to various NiO species formed mainly on the outer surface of the zeolite, peaks occurring in the range of 500-650 °C are due to Ni ions present inside the zeolitic channels and peaks located at temperatures higher than 700 °C are attributed to Ni species incorporated in the zeolitic network, according to the literature [41]. For YT5N sample, no reduction peak in temperature range of 500-650 °C was observed, which means that the microporous structure of the support did not allow the access of Ni ions inside the zeolitic channels with smaller dimensions than in the case of hierarchical zeolite. There is also a shift in the signals recorded for the hYT10N sample to higher values of reduction temperatures. This indicates stronger interactions between Ni oxide and supported titanium dioxide [42], most likely due to the high concentration of TiO_2 (10%) which ensures a higher probability of interaction with nickel oxide. The high degree of interaction between NiO and TiO_2 in this sample is also supported by the absence of reduction peaks of bulk NiO which usually occurs in the temperature range between 280-300 °C. In the case of a moderate interaction of NiO with TiO_2, its reduction takes place at about 400 °C, while in the case of stronger interactions with titanium dioxide, the reduction temperature of NiO increases to 530 °C [43, 44]. The presence of reduction peaks up to 500 °C for all the samples modified with Ti-Ni mixed oxides indicates the formation of NiO species, predominantly presented on the outer surface of zeolitic materials [42] (both zeolite Y and hierarchical zeolite hY). The consumption of hydrogen from temperatures higher than 600 °C can be attributed to the reduction of titanium. The presence of metallic nickel particles on the zeolite subsurface favors the molecular dissociation of H_2 and, thus, the reduction of Ti^{4+} to Ti^{3+} or Ti species with a lower valence state. The amount of hydrogen needed to reduce nickel is greater than the stoichiometric amount. This confirms the hypothesis that the reduction of small amounts of titanium also takes place.

Preprints (www.preprints.org) | NOT PEER-REVIEWED | Posted: 15 June 2023 doi:10.20944/preprints202306.1109.v1

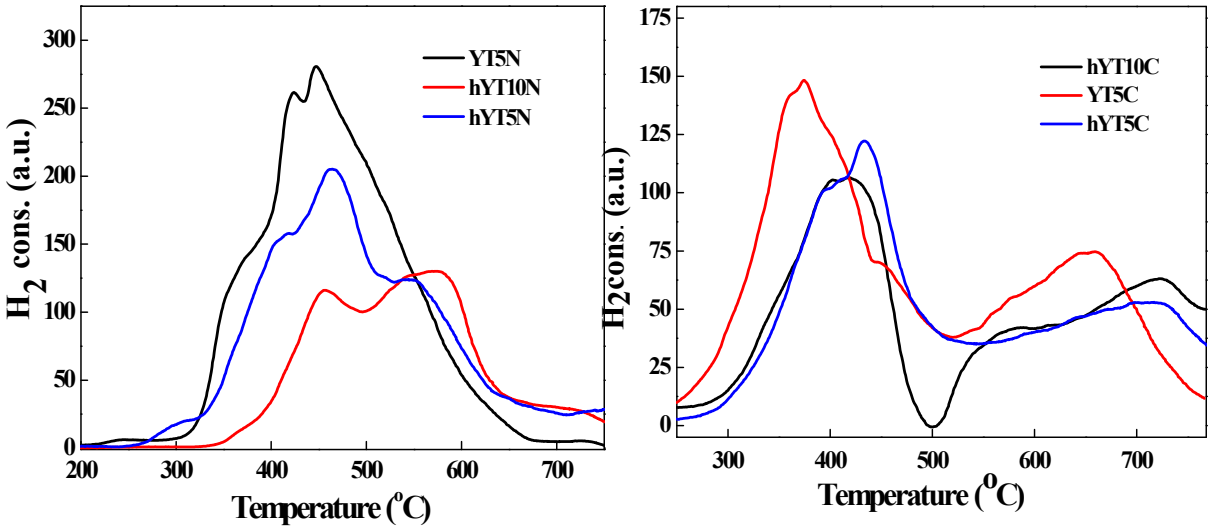

(a) (b)

Figure 6. H_2-TPR profiles of the samples with (a) Ti-Ni oxides, and (b) Ti-Co oxides.

Figure 6b shows the TPR profiles for Ti-Co containing samples with three different domains of reduction temperatures. The first peaks observed at lower temperature (200°C) correspond to the reduction to CoO on the surface of the support (I), second and third peaks located at 370 and 536°C (II and III) can be attributed to the reduction $Co^{3+} \rightarrow Co^{2+} \rightarrow Co^{0}$ and the fourth peak at 636°C can be attributed to the reduction of Co^{2+} which interacts strongly with the support [45-50]. TPR signals recorded at higher temperatures, between 600-700 °C are due to reduction of cobalt oxide species strongly bounded to the support (surface Co–O–Al species reduced to Co metal), as reported in the case of Co_3O_4 on alumina support [50].

3.1.6. XPS analysis

The surface of the samples and the oxidation states were investigated by XPS, which revealed the existence of the following core levels: O 1s, Si 2p, Al 2p, Na 1s, C 1s, Co 2p, Ti 2p and Ni 2p. The spectra of interest are illustrated in Fgure 7. The Table 3 gives the relevant parameters obtained after the deconvolutions of the core levels of interest (Ti 2p, Co 2p and Ni 2p): binding energies, amplitudes and an assignment by consulting the existing database. The deconvolutions highlight the coexistence of different oxides states, the ratio varying depending on the synthesis method (the incorporated titanium concentration).

Table 3. Binding energies (BE), amplitudes, and assignment of the deconvolutions for the core levels of interest for the samples.

Sample	Element		BE (eV)	Ampl. (cps)	Assignment
hYT2C	Ti2p	C1	456.06	84.85	Ti(II)
		C2	458.15	408.71	Ti(IV)
				Ti(III)/ Ti(IV)	0.21
	Co 2p	C1	778.92	480.6	Co(II)
		C2	780.88	214.7	Co(III)

Preprints (www.preprints.org) | NOT PEER-REVIEWED | Posted: 15 June 2023 doi:10.20944/preprints202306.1109.v1

				Co(III)/ Co(II)	0.45
YT5C	Ti 2p	C1	458.07	242.65	Ti(IV)
	Co 2p	C1	780.04	1229.39	Co(II)
		C2	781.65	471.77	Co(III)
				Co(III)/ Co(II)	0.38
hYT2N	Ti 2p	C2	456.04	77.38	Ti(III)
		C3	458.15	223.11	Ti(IV)
				Ti(III)/ Ti(IV)	0.35
	Ni 2p	C1	852.75	124.61	Ni(II)
		C2	854.5	673.48	Ni(III)
				Ni(II)/ Ni(III)	0.19

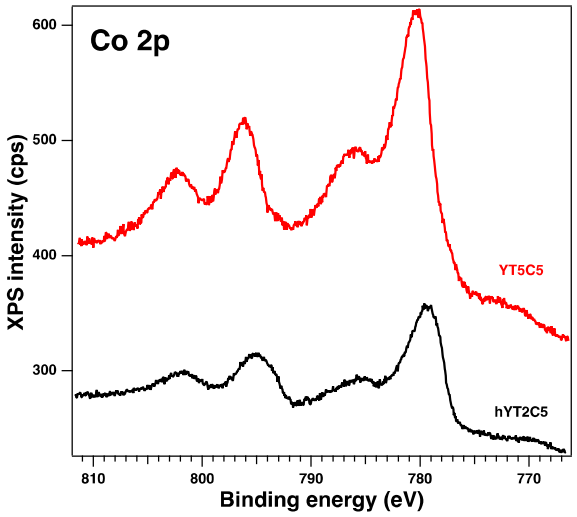

(a)

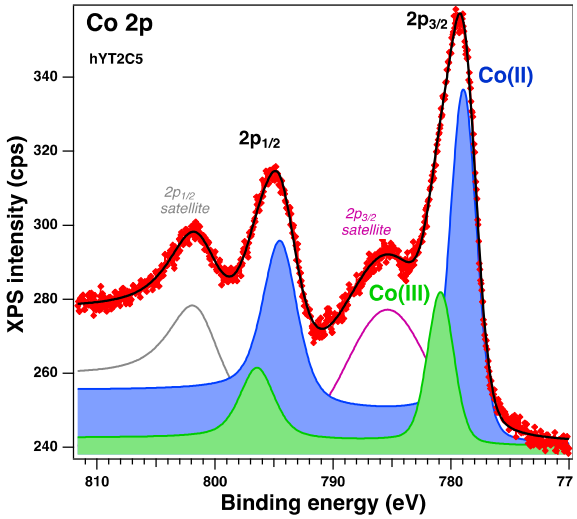

(b)

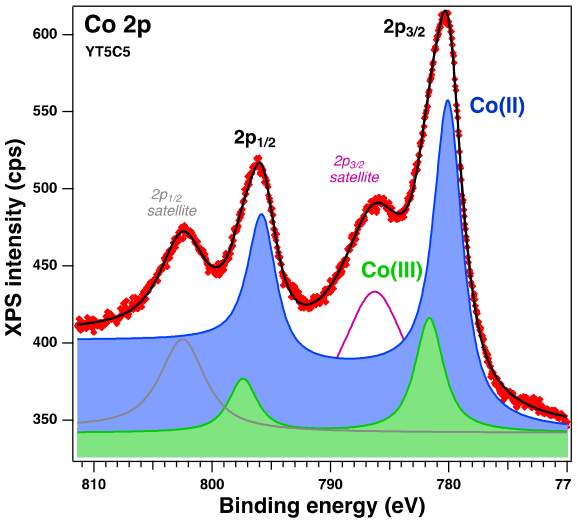

(c)

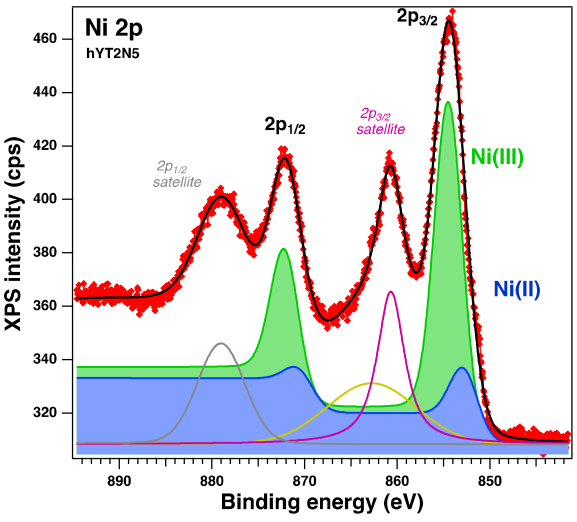

(d)

Preprints (www.preprints.org) | NOT PEER-REVIEWED | Posted: 15 June 2023 doi:10.20944/preprints202306.1109.v1

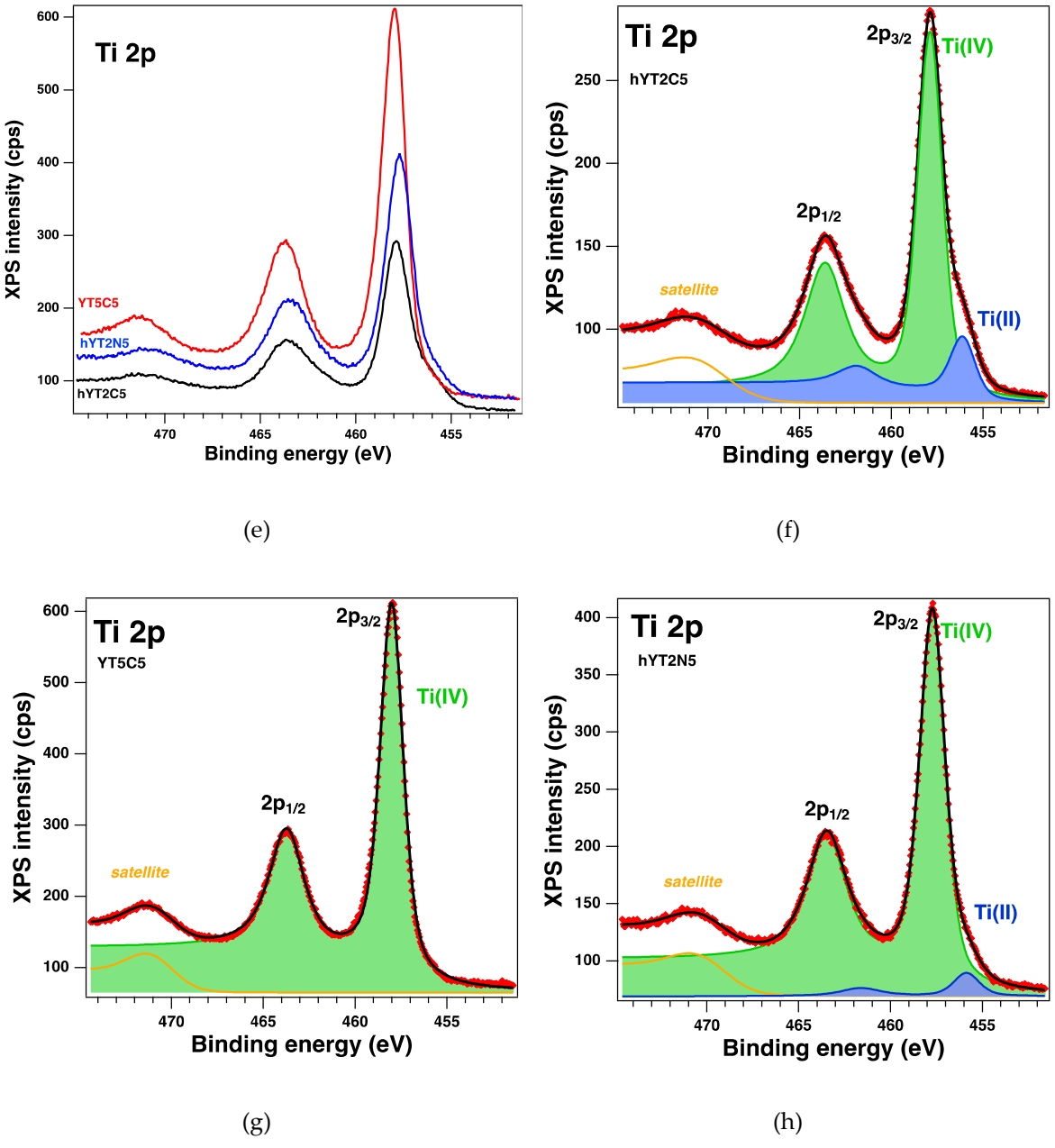

Figure 7. XPS spectra of the core levels Co 2p (a) for YT5C and hYT2C samples, and Ti 2p (e) for YT5C, hYT2C, and hYT2N doped samples, and (b-d, f-h) the fit and deconvolutions for the samples.

Thus, it can be observed that for sample YT5C, based on zeolite Y support, no titanium reduction occurs and the oxidized Co species are less (Table 3). Instead, the formation of Ti(III) is observed in the case of samples supported on hierarchical Y zeolite. At the same time, several species of oxidized Co (III) are formed on this support, even if the percentage of TiO_2 is lower. We consider that it is the result of different interactions of titanium species with the surface of zeolite Y and that of aluminosilicate with mesopores. However, comparing hYT2C and hYT2N samples that have the same support and percentage of TiO_2 and Co or Ni oxide, a significant increase in the amount of oxidized Ni (III) was observed, although the amount of reduced Ti (III) is slightly higher.

3.1.7. Raman spectroscopy

Raman spectra of the synthesized samples are illustrated in Figure 8. For Ti-Ni containing samples (Figure 8a), Raman modes of segregated anatase were depicted at 144 (E_g), 197 (E_g), 637 cm^{-1} (E_g) while for the samples modified with Ti and Co oxides, more obvious are the peaks located at

Preprints (www.preprints.org) | NOT PEER-REVIEWED | Posted: 15 June 2023 doi:10.20944/preprints202306.1109.v1

192, 483, 527, 620 and 692 cm^{-1} (Figure 8b) which characterize the Raman active modes of Co_3O_4. The phonon symmetries of these Raman peaks are caused by lattice vibrations of the spinel structure, in which Co^{2+} and Co^{3+} cations are situated at tetrahedral and octahedral sites in the cubic lattice [37].

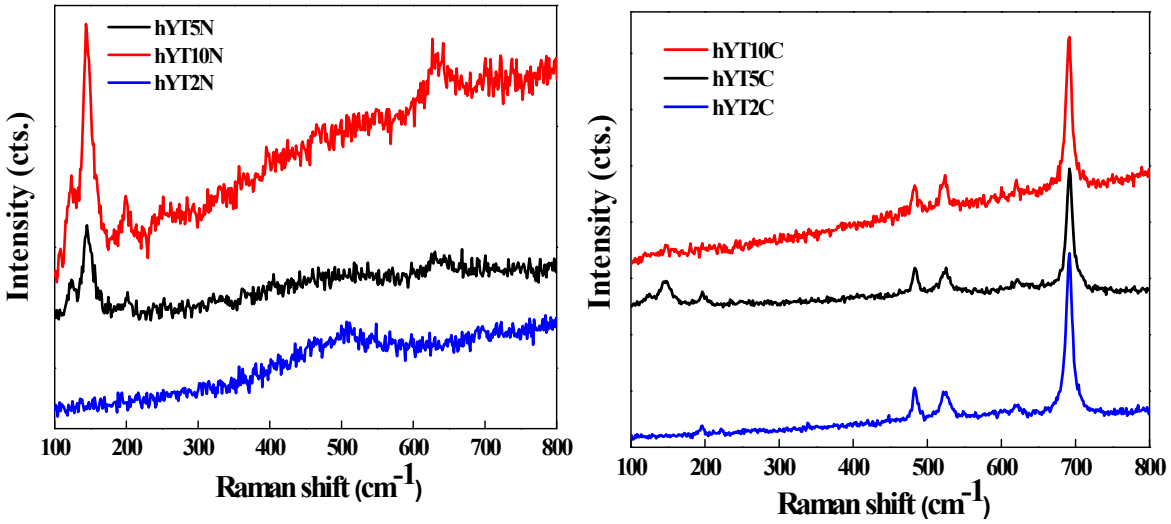

(a) (b)

Figure 8. Raman spectra of (a) hYT2N, hYT5N, hYT10N, and (b) hYT2C, hYT5C, hY110C samples.

3.2. Photocatalytic activity

3.2.1. Photocatalytic results

The synthesized materials were tested in the photocatalytic degradation of amoxicillin under UV and visible light irradiation. The results obtained are presented in Figure 9 (a-d). In the case of UV light irradiation (Figure 9a-b), it was observed a higher photocatalytic efficiency of materials based on hierarchical zeolite Y. This behavior is due to its characteristic properties which contribute to a high and uniform dispersion of metal species and also to improve the access of both light radiation and amoxicillin molecules to the metallic sites. Similar results were noticed under visible light irradiation (Figure 9c-d), highlighting that the hierarchical zeolite Y used as a support improves the photocatalytic performances of the resulted materials compared to the non-hierarchical zeolite Y.

Preprints (www.preprints.org) | NOT PEER-REVIEWED | Posted: 15 June 2023 doi:10.20944/preprints202306.1109.v1

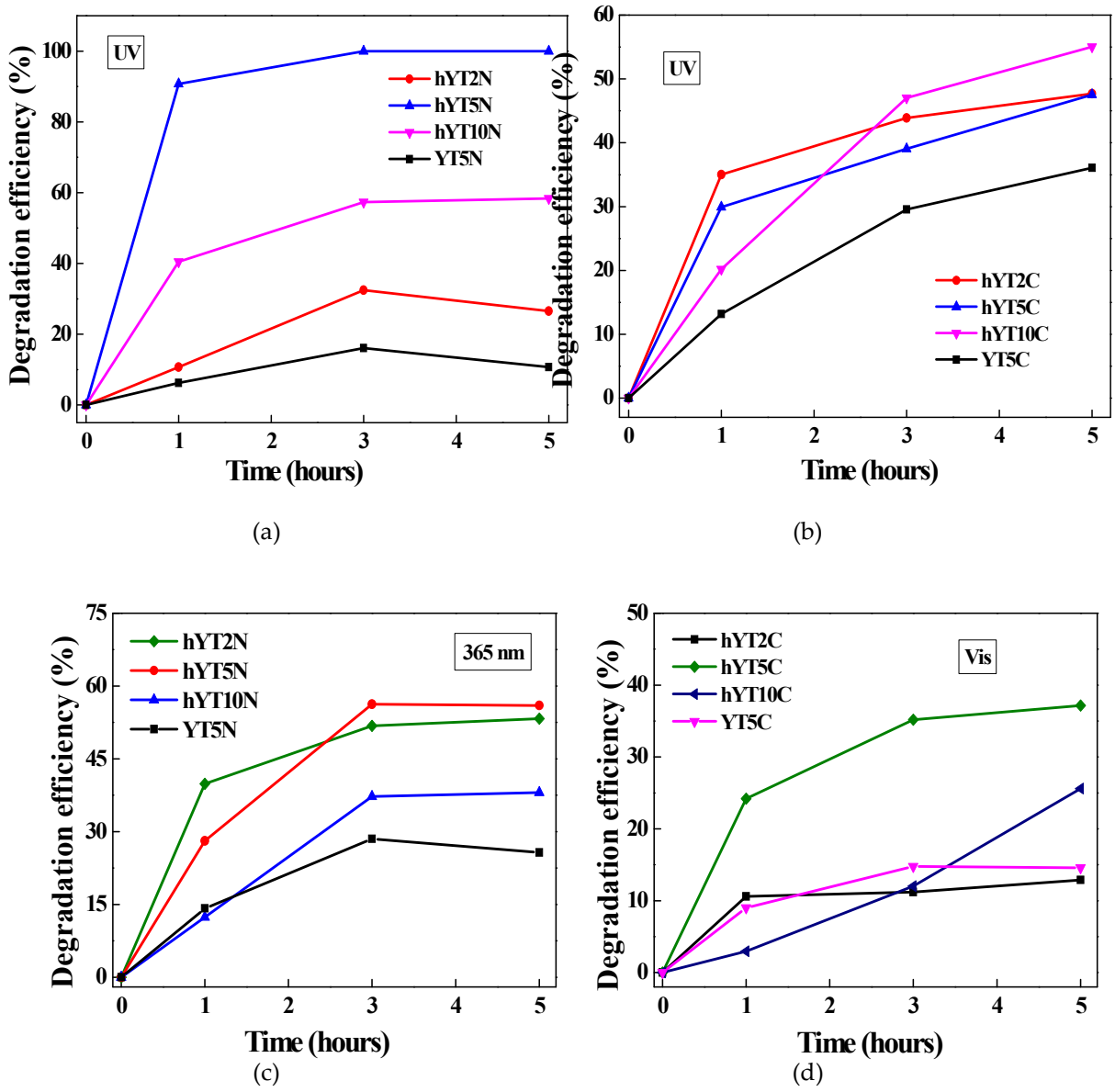

Figure 9. Photocatalytic degradation of amoxicillin using the synthesized materials under UV (a, b) and visible light (c, d) irradiation.

It was pointed out that Ti-Ni modified photocatalysts have better activity than those modified with Ti and Co oxides. It is explained by the efficient separation of photogenerated electron-hole pairs, as a synergistic effect of internal electric field resulted in a typical p-n heterojunction and band alignment of NiO and TiO_2 semiconductors, as can be seen in Figure 10a. In contrast, for the photocatalytic systems containing TiO_2-Co_3O_4, the electrons transfer across the electric field is thermodynamically hindered, because the conduction band of Co_3O_4 semiconductor is lower than that of TiO_2 (Figure 10b) [51].

Preprints (www.preprints.org) | NOT PEER-REVIEWED | Posted: 15 June 2023 doi:10.20944/preprints202306.1109.v1

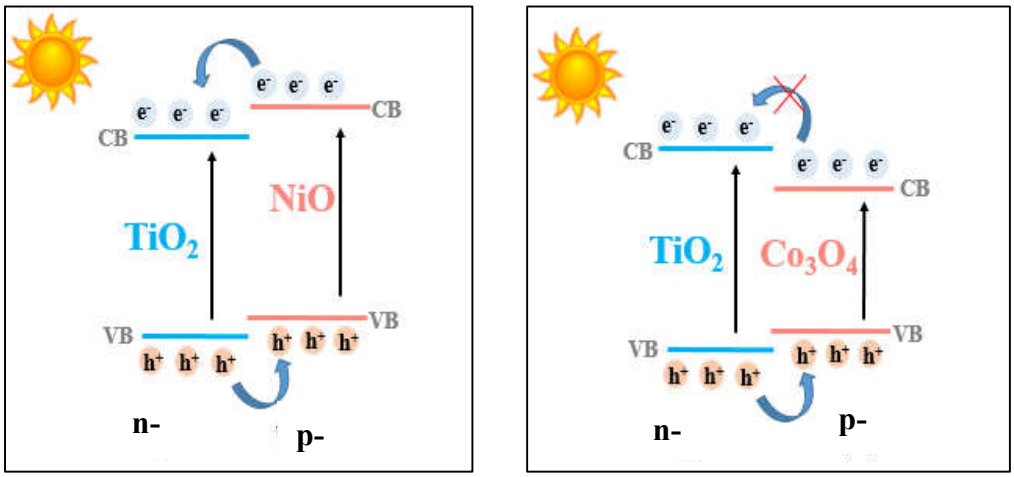

(a) (b)

Figure 10. Schematic representation of charge transfer in the p-n heterojunction of the synthesized materials.

A better separation of charge careers in the case of Ti-Ni samples leads to a higher number of holes available to generate more hydroxyl radicals (·OH), species responsible for the degradation of amoxicillin in photocatalytic reactions [16]. The ability of these materials to generate hydroxyl radicals was also supported by the fluorescence results obtained in the case of terephthalic acid reaction (Figure 11). This method is based on the capacity of terephthalic acid (TA) to interact with ·OH radicals resulted in aqueous solution during the photocatalytic experiment, leading to formation of a photoluminescence compound, 2-hydroxyterephthalic acid (TAOH) which can be quantified.

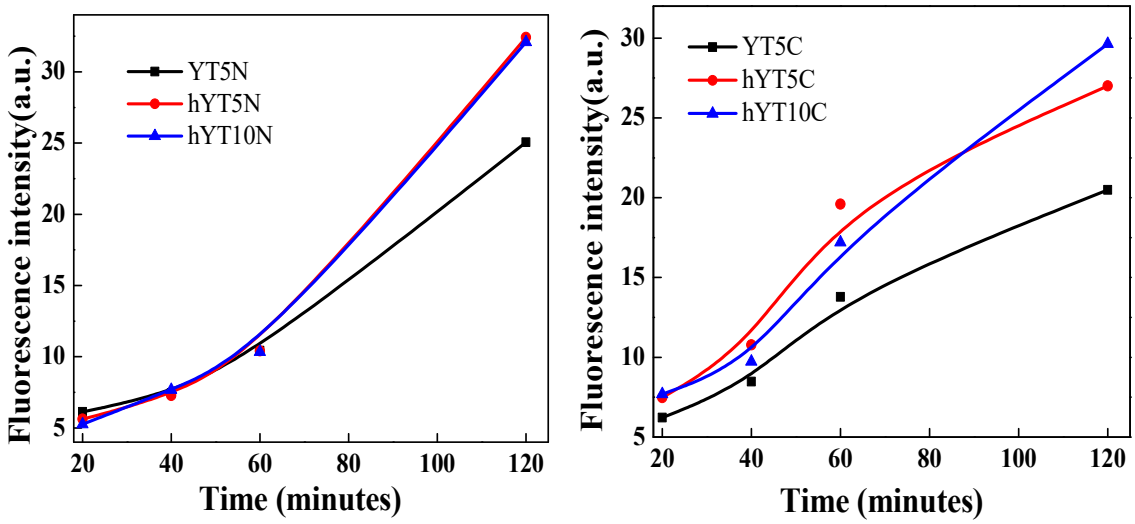

Figure 11. Fluorescence emission spectra of 2-hydroxyterephthalic acid resulted after interaction between terephthalic acid and ·OH radicals.

Preprints (www.preprints.org) | NOT PEER-REVIEWED | Posted: 15 June 2023 doi:10.20944/preprints202306.1109.v1

3.2.2. Mechanism investigations

Generally, the main reactive species in photocatalytic degradation of organic pollutants are hydroxyl (·OH), superoxide (·O_2^-) and holes (h^+) radicals [38]. To evaluate the mechanism of amoxicillin degradation using the synthesized materials, photocatalytic experiments were carried out in the presence of scavengers able to selectively interact with the highly reactive oxygen species (ROS) from the reaction system. The results obtained from these experiments are shown in Figure 12.

It was noticed a different contribution of reactive oxygen species to AMX degradation depending on the metal species used to modify the zeolitic support. Thus, in the case of the samples containing Ti and Ni oxides, the following order was observed h^+ >·O_2^->·OH while for the samples modified with Ti and Co oxides, the order was h^+ >·OH> ·O_2^-. The decrease in the degradation efficiency after KI addition suggests that holes are mainly responsible for AMX degradation. In fact, the holes have a dual role: they are directly involved in the degradation of amoxicillin molecules and in the formation of reactive hydroxyl species (·OH) through the oxidation of water.

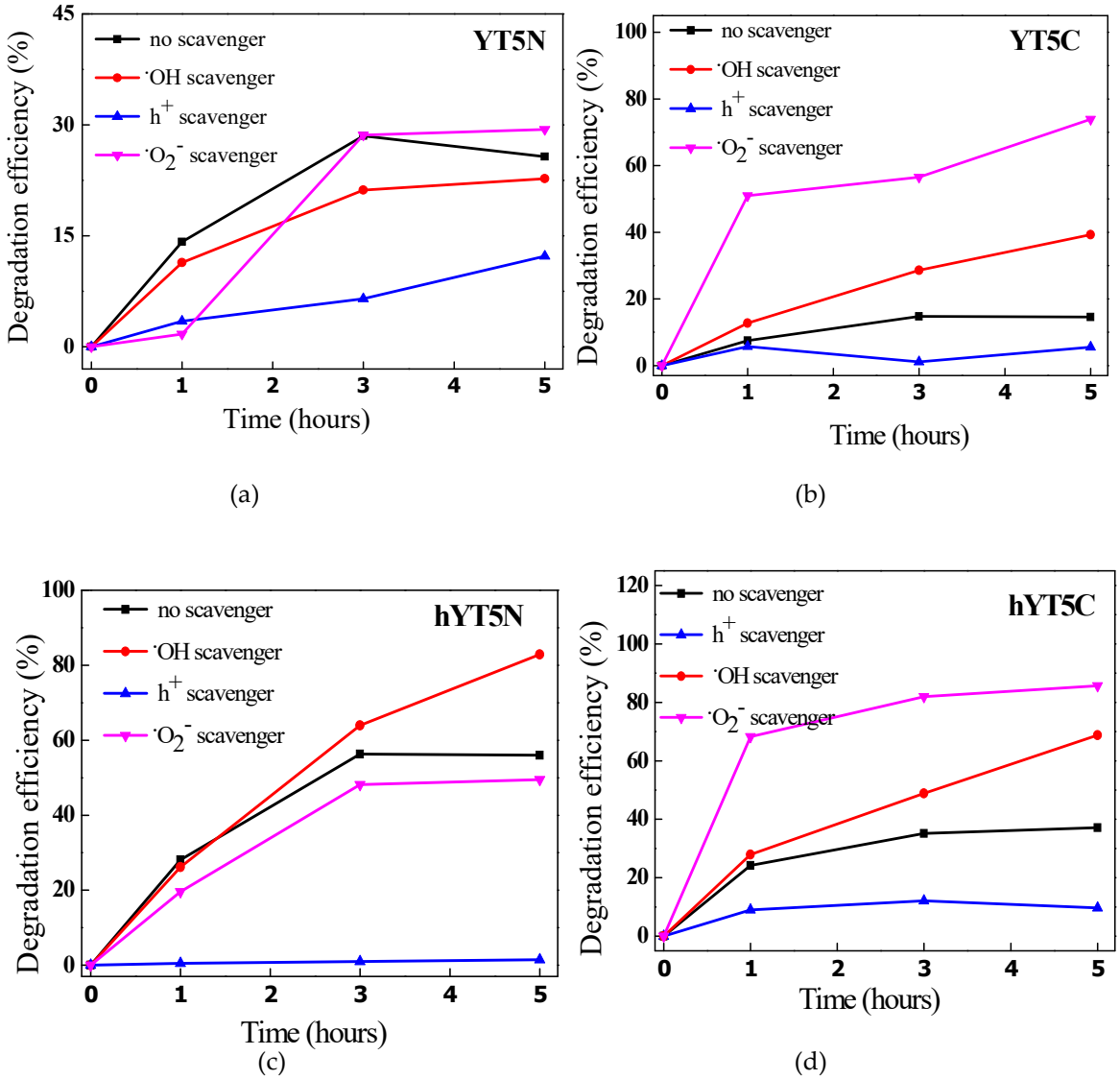

Preprints (www.preprints.org) | NOT PEER-REVIEWED | Posted: 15 June 2023 doi:10.20944/preprints202306.1109.v1

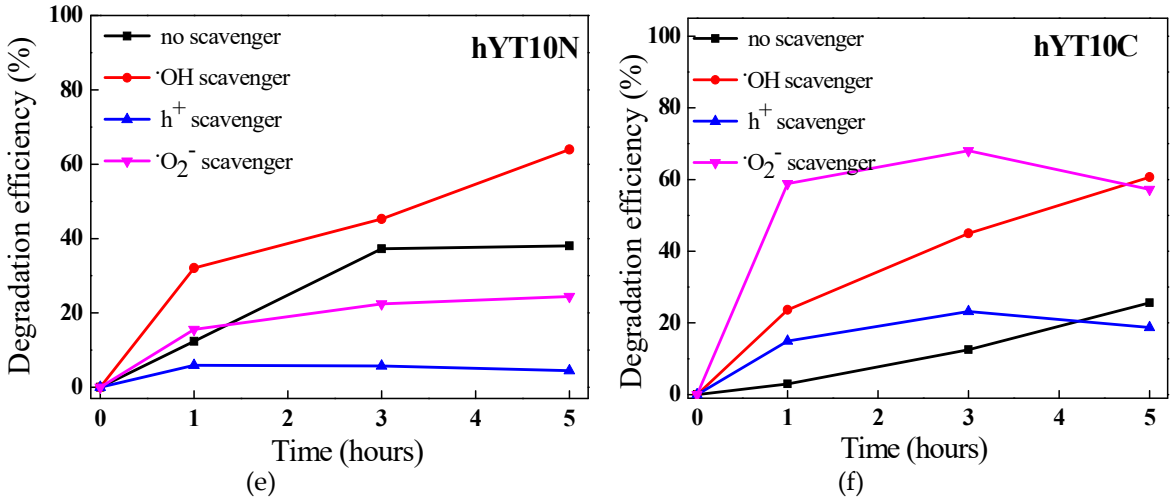

Figure 12. The effect of scavengers on the photocatalytic degradation of amoxicillin under visible light irradiation for (a) YT5N, (b) YT5C, (c) hYT5N, (d) hYT5C, (e) hYT10N, and (f) hYT10C samples.

Interesting is that by adding scavengers for $\cdot O_2^-$ and ·OH species, an increase of photocatytic efficiencies was recorded. It means that the lack of an active species in the system is compensated by the others with higher reactivity, depending on their oxidizing potential. For example, by capturing superoxide species, it is practically possible for amoxicillin molecules to be oxidized by hydroxyl radicals, known to be the most active of all reactive oxygen species [52], hence the increase in catalytic performance in the case of adding p-benzoquinone (p-BQ) in the system, as was obtained for the samples modified with titanium and cobalt oxides (Figure 12b,d,f).

4. Conclusions

New Co-Ti or Ni-Ti supported photocatalysts on zeolite Y with microporous and hierarchical structures were obtained and their high activity under UV and visible light was evidenced in amoxicillin photodegradation. A typical crystalline structure of zeolite Y and presence of mesopores were evidenced for all the obtained samples. A significant effect of the support was observed on Ti and Co/Ni species and their interaction. It was thus highlighted that the zeolite Y support stabilizes Ti in the 4+ oxidation state and reduces the oxidation of Co or Ni species. In the case of the hierarchical Y zeolite, reduced species of Ti (III) are formed on the surface, and the amount of the other oxidized metal species increases significantly in the case of nickel. The presence of Co and Ni species in 3+ and 2+ oxidation states was also confirmed by Raman spectroscopy and H_2-TPR results. The mechanism of amoxicillin degradation under UV and visible light irradiation, investigated in the presence of scavengers, evidenced the effect of metal species interaction and zeolite support. The best results were obtained for the immobilized Ni-Ti species and hierarchical zeolite Y support.

.

Author Contributions: Conceptualization, J.-L. B. and V.P.; Data curation, G.P., I.A., F.P., S.P., A.B., N.G.A., S.P. and L.R.; Formal analysis, F.P., N.G.A., L.R.; Investigation, G.P., I.A., F.P., S.P., A.B., N.G.A. and L.R.; Methodology, G.P., V.P and J.-L.B; validation, J.-L.B. and V.P.; writing—original draft preparation, G.P., F.P., N.G.A., J.-L.B. and V.P.; writing—review and editing, J.-L.B., G.P. and V.P.; visualization, J.-L. B, G.P. and V.P.; supervision, J.-L. B and V.P. All authors have read and agreed to the published version of the manuscript.

Funding: This research received no external funding.

Data Availability Statement: The data presented in this study are available on request from the corresponding author.

Conflicts of Interest: The authors declare no conflict of interest.

References

1. Zhao, Z.; Wang, N.; Zhang, H.; Shang, R.; Xing, J.; Zhang, D.; Li, J. Fabrication of ZSM-5 zeolite supported TiO2-NiO heterojunction photocatalyst and research on its photocatalytic performance, *J. Solid State Chem*. **2022**, 309, 122895. https://doi.org/10.1016/j.jssc.2022.122895
2. Umejuru, E. C.; Mashifana, T.; Kandjou, V.; Amani-Beni M.; Sadeghifar, H.; Fayazi, M.; Karimi-Maleh. H.; Sithole, N.T. Application of zeolite based nanocomposites for wastewater remediation: Evaluating newer and environmentally benign approaches, *Environ. Res*. **2023**, 231,116073. https://doi.org/10.1016/j.envres.2023.116073
3. Samaniego-Benítez,J.E.; García-García, A.; Rivera-Manrique, S.I.; Ramírez-Aparicio, J. Multiwalled carbon nanotubes/zeolite composite for dye degradation under sunlight, *Mater. Today Commun*. 2023, 35, 106046, https://doi.org/10.1016/j.mtcomm.2023.106046
4. Hu, G.; Yang, J.; Duan, X.; Farnood, R.; Yang, C.; Yang, J.; Liu, W.; Liu, Q. Recent developments and challenges in zeolite-based composite photocatalysts for environmental applications, *Chem. Eng. J*. **2021**,417, 129209. https://doi.org/10.1016/j.cej.2021.129209
5. Suraja,P.V.; Z. Yaakob, Z.; Binitha, N.N.; Resmi, M.R.; Silija, P.P. Photocatalytic degradation of dye pollutant over Ti and Co doped SBA-15: Comparison of activities under visible light, *Chem. Eng. J*. **2011**, 176– 177, 265– 271. https://doi:10.1016/j.cej.2011.05.071
6. Huang, C.H.; Chang, K.P.; Ou, H.D.; Chiang, Y.C.; Chang, E.E.; C.F. Wang, C.F. Characterization and application of Ti-containing mesoporous silica for dye removal with synergistic effect of coupled adsorption and photocatalytic oxidation, *J. Hazard. Mater*. **2011**, 186, 1174–1182. https://doi:10.1016/j.jhazmat.2010.11.125
7. Petcu, G.; Anghel, E.M.; Buixaderas, E.; Atkinson, I.; Somacescu, S.; Baran, A.; Culita, D.C.; Trica, B.; Bradu, C.; Ciobanu, M.; Parvulescu V. Au/Ti Synergistically Modified Supports Based on SiO2 with Different Pore Geometries and Architectures. Catalysts **2022**, 12, 1129. https://doi.org/10.3390/catal12101129
8. Petcu, G.; Anghel, E.M.; Somacescu, S.; Preda, S.; Culita, D.C.; Mocanu, S.; Ciobanu, M.; Parvulescu, V. Hierarchical Zeolite Y Containing Ti and Fe Oxides as Photocatalysts for Degradation of Amoxicillin, J. Nanosci. Nanotechnol. 2020, 1158–1169. https://doi:10.1166/jnn.2020.16981
9. Diban, N.; Pacuła, A.; Kumakiri, I.; Barquín, C.; Rivero, M.J.; Urtiaga, A.; Ortiz, I. TiO2–Zeolite Metal Composites for Photocatalytic Degradation of Organic Pollutants in Water, Catalysts **2021**, 11, 1367. https://doi.org/10.3390/catal11111367
10. Joseph, C.G. Sharain-Liew, Y.L, Bono A., Teng, L. Y. Photodegradation of Indigo Dye Using TiO_2 and TiO_2/Zeolite System, *Asian J. Chem.; **2013**, 25, 8402-8406,* http://dx.doi.org/10.14233/ajchem.2013.14768
11. Chatti, R.; Rayalu, S.S.; Dubey, N.; Labhsetwar, N.; Devotta,S.; Solar-based photoreduction of methyl orange using zeolite supported photocatalytic materials, *Sol. Energy Mater Sol. Cells*., **2007**, 180–190. http://dx.doi:10.1016/j.solmat.2006.08.009
12. Das, A.; Mrinal K. Adak, M.K.; Mahata, N.; Biswas, B. Wastewater treatment with the advent of TiO2 endowed photocatalysts and their reaction kinetics with scavenger effect, *J. Mol. Liq*. **2021**, 338, 116479. https://doi.org/10.1016/j.molliq.2021.116479
13. Chen, D.; Cheng, Y.; Zhou, N.; Paul Chen, P.; Wang, Y.; Kun Li, K.; Huo, S.; Cheng, P.; Peng, P.; Zhang, R.; Wang, L.; Liu, H.; Liu, Y.; Ruan, R.; Photocatalytic degradation of organic pollutants using TiO_2-based photocatalysts: A review, *J. Clean. Prod*. **2020**, 268, 121725. https://doi.org/10.1016/j.jclepro.2020.121725
14. Sescu, A.M.; Favier, L.; Lutic, D.; Soto-Donoso, N.; Ciobanu, G.; Harja, M. TiO2 Doped with Noble Metals as an Efficient Solution for the Photodegradation of Hazardous Organic Water Pollutants at Ambient Conditions. *Water* **2021**, 13, 19. https://dx.doi.org/10.3390/w13010019
15. Goncearenco, E.; Morjan, I.P.; Dutu, E.; Scarisoreanu, M.; Fleaca, C.; L. Gavrila-Florescu, L.; F. Dumitrache, F.; Banici, A.M.; Teodorescu, V.S.; Anastasescu, C., Sandulescu, A.; Balint, I.; The effect of noble metal addition on the properties of oxide semiconductors nanoparticles, J. Solid State Chem., 2022, 307, 122817, https://doi.org/10.1016/j.jssc.2021.122817
16. Krishnan, A.; Swarnalal, A.; Das, D., Krishnan, M.; Saji, V.S.; Shibli, S.M.A. A review on transition metal oxides based photocatalysts for degradation of synthetic organic pollutants, J. Environ. Sci. https://doi.org/10.1016/j.jes.2023.02.051
17. Amorós-Pérez, A.; Cano-Casanova, L.; Castillo-Deltell, A.; Lillo-Ródenas M.A.; Román-Martínez, M. C. TiO_2 Modification with Transition Metallic Species (Cr, Co, Ni, and Cu) for Photocatalytic Abatement of Acetic Acid in Liquid Phase and Propene in Gas Phase Materials 2019, 12, 40; https://doi:10.3390/ma12010040
18. Suligoj, A.; Arcon, I.; Mazaj,M.; Drazic, G.; Arcon, D.; Cool, P.; Stangar, U.L.; Tusar, N.N. Surface modified titanium dioxide using transition metals: nickel as a winning transition metal for solar light photocatalysis, *J. Mater. Chem. A*, **2018**, 6, 9882. https://doi.org/10.1039/c7ta07176k
19. FeTi- SBA-15 magnetic nanocomposites with photocatalytic properties Mihaela Filip a, Petcu, G.; Anghel, E.M.; Petrescu, S.; Trica, B., Osiceanu, P.; Stanica, N.; Atkinson, I.; Munteanu, C..; Mureseanu, M.; Parvulescu, V. *Catal. Today* **2021**, 366, 10–19. https://doi.org/10.1016/j.cattod.2020.08.003

20. Jo, W.-K.; Kumar, S.; Isaacs, A.A.; Lee, A. F.; Karthikeyan, S. Cobalt promoted TiO_2/GO for the photocatalytic degradation ofoxytetracycline and Congo Red, Appl. *Catal. B: Environ*. **2017**, 201 159–168. http://dx.doi.org/10.1016/j.apcatb.2016.08.022
21. Iwasaki, M.; Hara, M.; Kawada, H.; Tada*y*, H.; Ito, S.; Cobalt Ion-Doped TiO_2 Photocatalyst Response to Visible Light, *J. Colloid Interface Sci*. **2000,** 224**,** 202–204. http://dx. doi:10.1006/jcis.1999.6694
22. Akel, S.; Boughaled, R.; Dillert, R.; El Azzouzi, M.; Bahnemann, D.W. UV/Vis Light Induced Degradation of Oxytetracycline Hydrochloride Mediated by Co-TiO_2 Nanoparticles. *Molecules* **2020**, 25, 249. http://dx. doi:10.3390/molecules25020249
23. Li, J.; Liu, S.; He, Y.; Wang, J. Adsorption and degradation of the cationic dyes over Co doped amorphous mesoporous titania–silica catalyst under UV and visible light irradiation, *Microporous Mesoporous Mater*. **2008**, 115, 416–425. https://doi.org/10.1016/j.micromeso.2008.02.022
24. Najafabadi, A.T.; Taghipour, F. Cobalt precursor role in the photocatalytic activity of the zeolite-supported TiO_2-based photocatalysts under visible light: A promising tool toward zeolite-based core–shell photocatalysis, *J. Photochem. Photobiol. A: Chem*. **2012**, 248, 1– 7. http://dx.doi.org/10.1016/j.jphotochem.2012.07.015
25. Song, Z.; Liu, J.; Hu, Y.; Li, S.; Zhang, X.; Ma,L.; Chen, L.; Zhang, Q. Solvent-controlled selective photocatalytic oxidation of benzyl alcohol over Ni@C/TiO_2, *Catal. Commun.* **2023**, 176, 106628. https://doi.org/10.1016/j.catcom.2023.106628
26. Zhao, Z.; Wang, N.; Zhang, H.; Shang, R.; Xing, J.; Zhang, D.; Li, J. Fabrication of ZSM-5 zeolite supported TiO_2-NiO heterojunction photocatalyst and research on its photocatalytic performance, *J. Solid State Chem.* **2022**, 309, 122895, https://doi.org/10.1016/j.jssc.2022.122895
27. Lu,X.; Liu, F.; Dang, Y.; Li, M.; Ruan, M.; Wu, M.; Zhu C.; Mani, T.; Suib, S.L.; Gao, P.-X. Transition-metal doped titanate nanowire photocatalysts boosted by selective ion-exchange induced defect engineering , *Appl. Surf. Sci*. **2022**, 591, 153116. https://doi.org/10.1016/j.apsusc.2022.153116
28. Daia, G.; Liua, S.; Lianga, Y.; Luo, T. Synthesis and enhanced photoelectrocatalytic activity of p–n junction Co_3O_4/TiO_2 nanotube arrays, *Appl. Surf. Sci.* **2013**, 264, 157– 161, http://dx.doi.org/10.1016/j.apsusc.2012.09.160
29. Chen, J.; Wang, M.; Han, J.; Guo, R. TiO_2 nanosheet/NiO nanorod hierarchical nanostructures: p–n heterojunctions towards efficient photocatalysis, *J. Colloid Interface Sci*. **2020**, 562, 313–321. https://doi.org/10.1016/j.jcis.2019.12.031
30. Uddin, T.; Nicolas, Y.; C. Oliver, C.; Jaegermann, W.; Rockstroh, N.; Junge H.; Toupance, T. Band alignment investigations of heterostructure NiO/TiO_2 nanomaterials used as efficient heterojunction earth-abundant metal oxide photocatalysts for hydrogen production, *Phys. Chem. Chem. Phys.*, **2017**, https://doi.org/10.1039/C7CP01300K**.**
31. Tseng, Y.-H.; Huang, B.-K. Photocatalytic Degradation of NO_x Using Ni-Containing TiO_2, *Int. J. Photoenergy*. **2012**, https://doi:10.1155/2012/832180
32. Teodorescu, C.M.; Esteva, J.M.; Karnatak, R.C.; El Afif, A. An approximation of the Voigt I profile for the fitting of experimental x-ray absorption data. *Nucl. Instrum. Meth. Phys. Res. A* **1994**, 345, 141-147.
33. Shindo,T.; Koizumi, N.; Hatekeyama, K.; Ikeuchi, T. Post-synthesis of TiO_2 Dispersed Inside the Pore Channels of SBA-15 and its Photocatalytic Activity for the Degradation of Methylene Blue. *Int. J. Soc. Mater. Eng. Resour*. **2011**, 18, 11-17. https://doi.org/10.5188/ijsmer.18.11
34. Ziebro,J.; Łukasiewicz, I.; Borowiak-Palen, E.; Michalkiewicz, B. Low temperature growth of carbon nanotubes from methane catalytic decomposition over nickel supported on a zeolite, Nanotechnol. **2010**, 21, 145308. https://doi.org/10.1088/0957-4484/21/14/145308
35. Sacaliuc, E.; Beale, A.M.; Weckhuysen, B.M.; Nijhuis, T.A. Propene epoxidation over Au/Ti-SBA-15 catalysts, *J. Catal.* **2007,** 248, 235-248. https://doi.org/10.1016/j.jcat.2007.03.014
36. Yadav, R.; Amoli, V.; Singh, J.; Tripathi, M.K.; Bhanja, P.; Bhaumik, A.; Sinha, A.K. Plasmonic gold deposited on mesoporous TixSi1-xO2 with isolated silica in lattice: An excellent photocatalyst for photocatalytic conversion of CO_2 into methanol under visible light irradiation. *J. CO2 Util.* **2018**, 27, 11–21. https://doi.org/10.1016/j.jcou.2018.06.016
37. Ravindra, A.V.; Behera, B.C.; Padhan, P. Laser Induced Structural Phase Transformation of Cobalt Oxides Nanostructures**,** *J. Nanosci. Nanotechnol.* **2014**, 14, 5591-5595. https://doi.org/10.1166/jnn.2014.9023
38. Xu, X.; Sun, Y.; Fan, Z.; Zhao, D.; Xiong, S.; Zhang, B.; Zhou, S.; Liu, G. Mechanisms for $\cdot O^{-}_2$ and ·OH Production on Flowerlike BiVO4 Photocatalysis Based on Electron Spin Resonance, *Front. Chem.* **2018**, 6, 64, https://doi.org/10.3389/fchem.2018.00064.
39. Graca, I.; González, L.V.; Bacariza, M.C.; Fernandes, A.; Henriques, C.; Lopes, J.M.; Ribeiro, M.F. CO_2 hydrogenation into CH_4 on NiHNaUSY zeolites**,** *Appl. Catal. B: Environ.* **2014**, 147, 101-110. https://doi.org/10.1016/j.apcatb.2013.08.010
40. Iwasaki, M.; Hara, M.; Kawada, H.; Taday, H.; Ito, S. Cobalt Ion-Doped TiO2 Photocatalyst Response to Visible Light, J. Colloid Interface Sci. **2000,** 224, 202-207. https://doi.org/10.1006/jcis.1999.6694.
41. Lin, T.J.; Meng, X.; Shi, L. Ni-exchanged Y-zeolite- An efficient heterogeneous catalyst for acetylene hydrocarboxylation, *Appl. Catal. A* **2014**, 485, 163–171. https://doi.org/10.1016/j.apcata.2014.07

42. Mohan, V.; Raghavendra, C.; Pramod, C.V.; Raju, B.D.; Rao, K.S.R. Ni/H-ZSM-5 as a promising catalyst for vapour phase hydrogenation of levulinic acid at atmospheric pressure, *RSC Adv.* **2014**, 4, 9660. https://doi.org/10.1039/c3ra46485g
43. Deshmane, V.G.; Owen, S.L.; Abrokwah, R.Y.; Kuila, D. Mesoporous nanocrystalline TiO_2 supported metal (Cu, Co, Ni, Pd, Zn,and Sn) catalysts: Effect of metal-support interactions on steamreforming of methanol, *J. Mol. Catal A* **2015**, 408, 202–213. http://dx.doi.org/10.1016/j.molcata.2015.07.023
44. Ivan, S.B.; Fechete, I.; Papa, F.; Marcu, I.C. Ethane oxydehydrogenation over TiP_2O_7-supported NiO catalysts, *Catal. Today* **2021**, 366, 133-140. https://doi.org/10.1016/j.cattod.2020.02.005
45. Jongsomjit, B.; Panpranot, J.; Goodwin, J.G. Jr. Co-support compound formation in alumina-supported cobalt catalysts, *J. Catal.* **2001**, 204, 98-109. https://doi.org/10.1006/jcat.2001.3387
46. Zhang, Y.; Wei ,D.; Hammache, S.; Goodwin, J.G. Jr. Effect of Water Vapor on the Reduction of Ru-Promoted Co/Al_2O_3, *J. Catal.* **1999**, 188, 281–290. https://doi.org/10.1006/jcat.1999.2666
47. Srisawad, N.; Chaitree, W.; Mekasuwandumrong, O.; Shotipruk, A.; Jongsomjit, B.; Panpranot, J. CO2 hydrogenation over Co/Al_2O_3 catalysts prepared via a solid-state reaction of fine gibbsite and cobalt precursors, *Reac Kinet Mech Cat* **2012,** 107, 179–188. https://doi.org/10.1007/s11144-012-0459
48. Ji, Y.; Zhao, Z.; Duan, A.; Jiang, G.; Liu, J. Comparative Study on the Formation and Reduction of Bulk and Al2O3-Supported Cobalt Oxides by H2-TPR Technique, *J. Phys. Chem. C* **2009**, 113, 7186–7199. https://doi.org/10.1021/jp8107057
49. Kruatim, J.; Jantasee, S.; Jongsomjit, B. Improvement of Cobalt Dispersion on Co/SBA-15 and Co/SBA-16 Catalysts by Ultrasound and Vacuum Treatments during Post-Impregnation Step, *Eng. J.* **2017**, 21, 17-28. https://doi.org/10.4186/ej.2017.21.21.17
50. Solsona, B.; Davies, T.E.; Garcia, T.; Vazquez, I.; Dejoz, A. Taylor, S.H. Total oxidation of propane using nanocrystalline cobalt oxide and supported cobalt oxide catalysts, *Appl. Catal. B* **2008**, 84, 176–184. https://doi.org/10.1016/j.apcatb.2008.03.021
51. Liu, L.; Li, Y. Understanding the Reaction Mechanism of Photocatalytic Reduction of CO_2 with H_2O on TiO_2-Based Photocatalysts: A Review, *Aerosol Air Qual. Res.* **2014,** 14, 453–469. https://doi.org/10.4209/aaqr.2013.06.0186
52. Collin, F. Chemical Basis of Reactive Oxygen Species Reactivity and Involvement in Neurodegenerative Diseases**,** *Int. J. Mol. Sci.* **2019,** 20, 2407. https://doi.org/10.3390/ijms20102407.